Supplementary Information:

Perfect acoustic bandgap meta-beam based on a quadruple-mode resonator array

Kentaro Fujita, Motonobu Tomoda, Oliver B. Wright, and Osamu Matsuda

Division of Applied Physics, Graduate School of Engineering, Hokkaido University, Sapporo 060-8628, Japan

Abstract

We describe here the approximate analytical or semi-analytical models used to describe the meta-beam unit-cell resonant frequencies, the effect of the unit-cell frame thickness on the position and width of the band gap, the details of the experimental setups and measurements, and the details of the numerical simulations.

1 Approximate analytical models of the quadruple-mode meta-beam resonator

The geometry of the fabricated meta-beam is shown in Fig. S1. We first explain in detail the analytical model for the unit-cell compressional resonance and then for the other three modes.

1.1 Compressional resonance

The analytical model for the compressional resonance is shown in Fig. S2(a). When the inner mass moves and a load force F is applied to the right-hand end of spring 2 in the y direction, this spring deforms as shown in Fig. S2(b). Euler-Bernoulli beam theory [1] allows one to calculate the y-directed bending deformation $h(x)$ of the bar (for $0 < x < l_1$):

$$\frac{d^3h}{dx^3} + \frac{F}{EI_1^{(\mathrm{a})}} = 0, \qquad \left(I_1^{(\mathrm{a})} = \frac{d_1^3 t}{12}\right) \tag{S1}$$

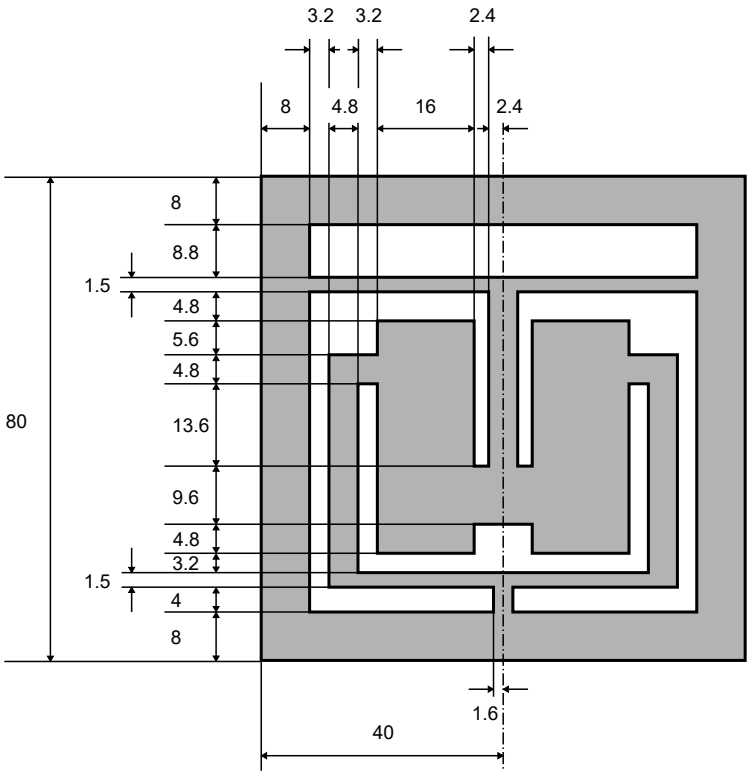

Figure S1: Details of the meta-beam unit cell of thickness 8 mm. The numerical values are in mm. The structure is symmetric with respect to the center dotted-dashed line.

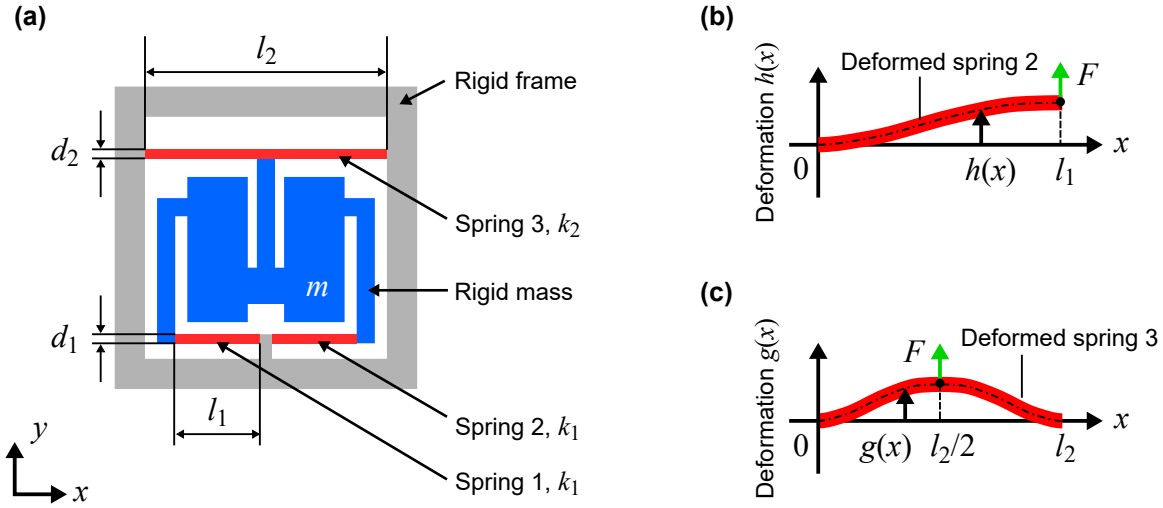

Figure S2: Approximate analytical model for the compressional resonance of a single unit-cell. (a) Geometry. The blue region and red ribs are a rigid inner mass and (leaf) springs, respectively, corresponding to motion along the beam axial direction, and the grey regions are considered to be a rigid frame. The mass oscillates along the axial direction. (b) Deformation of the spring 2 with an applied force F. The thick red curve corresponds to the bent configuration. The black dotted-dashed line is the neutral surface. (c) Deformation of the spring 3, with similar notation.

where $I_1^{(\mathrm{a})}$ is the moment of area of spring 2, and

$$h(x) = -\frac{F}{6EI_1^{(\mathrm{a})}}x^3 + C_1x^2 + C_2x + C_3, \tag{S2}$$

where E is the Young's modulus and C_i $(i = 1, 2, 3)$ are unknown constants. The rigid connection of the spring 2 at $x = 0$ leads to the boundary conditions $dh(0)/dx = 0, h(0) = 0$, so that $C_2 = 0, C_3 = 0$. The bending angle at $x = l_1$ is therefore also zero, because we assume that all the springs are rigidly connected to the mass and that the mass only moves in the axial direction. The assumption $dh(l_1)/dx = 0$ implies $C_1 = Fl_1/4EI_1^{(\mathrm{a})}$, leading to

$$h(x) = -\frac{F}{6EI_1^{(\mathrm{a})}}x^3 + \frac{F}{4EI_1^{(\mathrm{a})}}l_1x^2, \tag{S3}$$

where the spring constant k_1 is given by

$$k_1 = \frac{F}{h(l_1)} = \frac{12EI_1^{(\mathrm{a})}}{l_1^3} = \frac{Ed_1^3t}{l_1^3}. \tag{S4}$$

The spring constant of spring 3 is similarly derived by considering two half springs in parallel:

$$k_2 = \frac{16Ed_2^3t}{l_2^3}. \tag{S5}$$

The predicted frequency for the compressional resonance based on these spring constants and choice of inner mass, ignoring the mass of the springs, is given in the main text.

1.2 Torsional resonance

An analytical model for the torsional resonance is shown in Fig. S3. Two torsional springs 1 and 2 are included in the system. The torsional constant, length, and width of these are K_i, l_i, d_i, respectively, where $i = 1, 2$ for springs 1, 2. (These symbol definitions for each mode should be considered separately in each of the sub-sections 1.1 to 1.4.) The equation for torsional motion is

$$I\frac{d^2\theta}{dt^2} + K\theta = 0, \tag{S6}$$

where I, θ are the moment of inertia of the inner mass and the rotation angle, respectively, ignoring the moment of inertia of the springs. For a rectangular bar,

$$K = \frac{GJ(d, t)}{l}, \tag{S7}$$

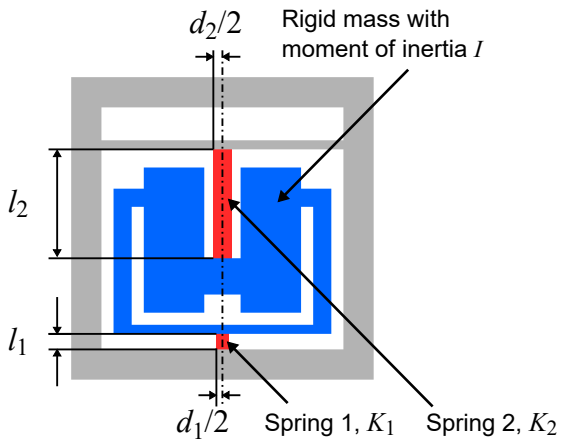

Figure S3: Approximate analytical model for the torsional resonance of a single unit-cell. The blue region and red ribs are a rigid inner mass and torsional springs, respectively, and the the grey regions are a rigid frame. The mass oscillates about the central dotted-dashed rotation axis.

where G is the shear rigidity and

$$J(d,t) = \frac{1}{3}d^3t\left[1 - \frac{192}{\pi^5}\frac{d}{t}\sum_{n=1}^{\infty}\frac{1}{(2n-1)^5}\tanh\frac{(2n-1)\pi t}{2d}\right]. \tag{S8}$$

The quantities l, d and t are the length, width and thickness of the bar, with $t > d$ [2]. In our case,

$$K_1 = \frac{GJ(d_1,t)}{l_1} = 1.75 \times 10^2 \text{ Nm}, \tag{S9}$$

$$K_2 = \frac{GJ(d_2,t)}{l_2} = 4.47 \times 10^2 \text{ Nm}, \tag{S10}$$

where $d_1 = 4.8$ mm, $d_2 = 3.2$ mm, $t = 8$ mm, $l_1 = 28.8$ mm, $l_2 = 4$ mm, $J(d_1,t) = 1.85 \times 10^{-10}$ m^4, $J(d_2,t) = 6.54 \times 10^{-11}$ m^4, $G = 27.3$ GPa. We obtain $I = 1.19 \times 10^{-5}$ kg m^2. Since the two springs are connected in series, the resonant frequency is predicted to be

$$f = \frac{1}{2\pi}\sqrt{\frac{K_1 + K_2}{I}}, \tag{S11}$$

giving f=1150 Hz. The value from simulation is f=980 Hz. The difference mainly stems from the approximation that the springs are connected to rigid bodies, increasing f.

1.3 Shear-horizontal resonance

An analytical model for the shear-horizontal resonance is shown in Fig. S4, involving three springs 1-3. The rigid inner mass m swings about the center of rotation O shown in Fig. S4(b). Judging from the results of the simulation, this point is 0.2 mm directly below the point shown in Fig. S4(b), but we ignore this small distance in the following discussion. The identical springs 1 and 2 have length and width l_1 and d_1, respectively, whereas for spring 3 they are l_2 and d_2. The shortest distance between the springs 1 and 2 is d_3, the distance from O to

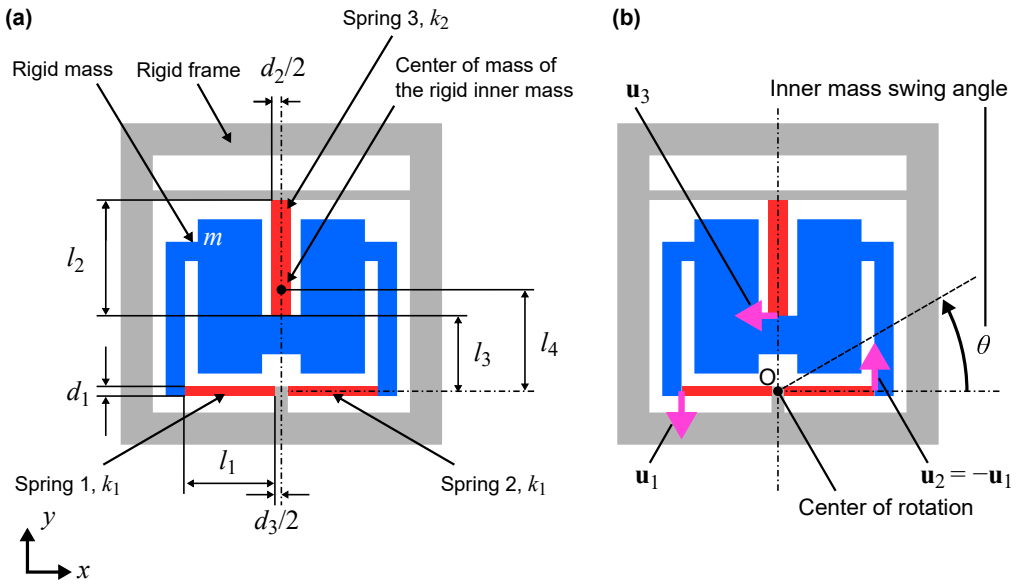

Figure S4: Approximate analytical model for the shear-horizontal resonance of a single unit-cell. (a) Geometry. The blue region and red ribs are a rigid inner mass and flexural springs, respectively, and the grey regions are a rigid frame. (b) Schematic diagram of the displacements. The mass oscillates about the center of rotation O. The pink arrows indicate the displacement vector of one end of each spring.

the bottom end of spring 3 is l_3, and the distance from O to the center of mass of the rigid inner mass is l_4. We assume that one end of the each spring is fixed rigidly whereas the other is connected to the laterally swinging mass. The displacement of the end of each spring 1, 2 and 3 is given by

$$\mathbf{u}_1 = -\mathbf{u}_2 = -\theta \left(l_1 + \frac{d_3}{2} \right) \mathbf{j}, \tag{S12}$$

$$\mathbf{u}_3 = -\theta l_3 \mathbf{i}, \tag{S13}$$

respectively, where θ is the rotation angle and the unit vectors $\mathbf{i}, \mathbf{j}$ correspond to the x, y directions, respectively. We shall assume that $|\theta| \ll 1$, so that second- or higher-order terms in θ are negligible. When the moment of inertia of the inner mass is ignored, the equation of motion is given by

$$m l_4 \ddot{\theta} + 2k_1 (l_1 + \frac{d_3}{2})\theta + k_2 l_3 \theta = 0, \tag{S14}$$

where k_1 and k_2 are the bending spring constants of the springs 1 (equal to that of 2) and 3, respectively, and the center of mass of the inner mass is displaced laterally by $-\theta l_4 \mathbf{i}$. The above equation can be transformed to

$$m\ddot{\theta} + \left(2k_1 \frac{l_1 + d_3/2}{l_4} + k_2 \frac{l_3}{l_4} \right) \theta = 0. \tag{S15}$$

Spring constants k_1, k_2, similar to the (leaf) springs considered for the compressional mode, can be considered as cantilever spring constants:

$$k_i = \frac{E d_i^3 t}{4 l_i^3} \qquad (i = 1, 2). \tag{S16}$$

Thus, the resonant frequency for the shear-horizontal mode is given by

$$f = \frac{1}{2\pi}\sqrt{\frac{2k_1\frac{l_1+d_3/2}{l_4} + k_2\frac{l_3}{l_4}}{m}}. \tag{S17}$$

Using $l_1 = 22.4$ mm, $l_2 = 28.8$ mm, $l_3 = 17.6$ mm, $l_4 = 20.9$ mm, $d_1 = 2.4$ mm, $d_2 = 4.8$ mm, $d_3 = 3.2$ mm, $m = 3.84\times10^{-2}$ kg, $E = 73.1$ GPa, we obtain f=806 Hz in fairly good agreement with the value from simulation f=990 Hz. The difference stems mainly from the approximations concerning the boundary conditions of the springs. Moreover, the inner mass also vibrates horizontally in the x direction in the simulation, something that is ignored in the analytical model.

1.4 Shear-vertical resonance

A semi-analytical model for the shear-vertical resonance is shown in Fig. S5. The rigid inner mass m is suspended by three springs, i.e. two L-shaped springs 1 and 2 whose spring constants are k_1 and one T-shaped spring 3 whose spring constant is k_2. We assume that these springs only bend vertically, i.e. the green portions A, B and C in Fig. S5 show zero displacement in the x and y directions. The spring constants for k_1 and k_2 we obtain using finite-element simulation by loading a vertical force on the faces A, B and C in the simulations subject to the above constraints and noting the displacements: $k_1 = 5.9 \times 10^5$ N m^{-1}, $k_2 = 1.3 \times 10^6$ N m^{-1}. The corresponding semi-analytically predicted resonant frequency is $f = (1/2\pi)\sqrt{(2k_1 + k_2)/m} = 1440$ Hz, where $m = 3.02 \times 10^{-2}$ kg, which should be compared with the value f=1010 Hz from the simulation of a single unit-cell resonant frequency. The difference is significantly larger than for the other modes, presumably because the semi-analytically derived resonant frequency is highly sensitive to the boundary conditions of the three springs.

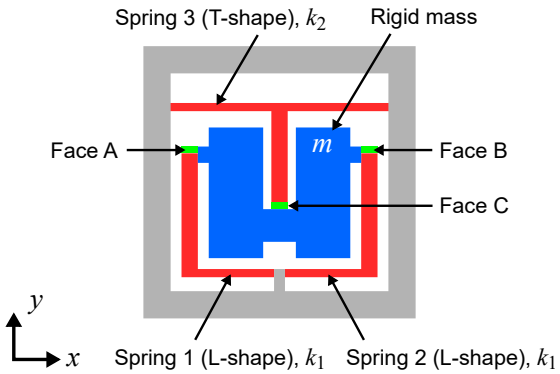

Figure S5: Approximate semi-analytical model for the shear-vertical resonance of a single unit-cell. The blue region and red ribs are a rigid inner mass and flexural springs, respectively, and the the grey regions are a rigid frame. Springs 1 and 2 are L-shaped, whereas spring 3 is T-shaped. The light green lines on these springs indicate specific spring ends. The mass oscillates in the out-of-plane direction in this figure.

2 Effect of the outer frame thicknesses

In order to investigate the effect of the outer frame geometry on the dispersion relation, we vary the thicknesses as shown in Fig. S6. The axial and horizontal thicknesses are defined as t_a and t_h, respectively. Figure S7 shows the variation of the band gaps and single-cell resonances on varying t_a and t_h in the range 8±4 mm away from their design value of 8 mm. Considerable variations in the band gaps is seen. In general, the gaps become

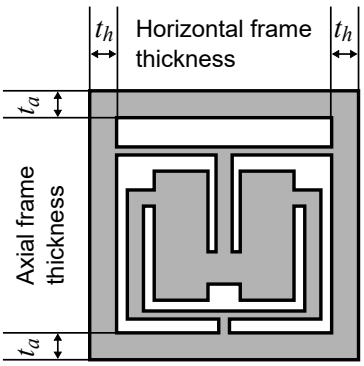

Figure S6: Geometry for the frame thickness changes, showing the definitions of the axial and horizontal thicknesses t_a and t_h, respectively.

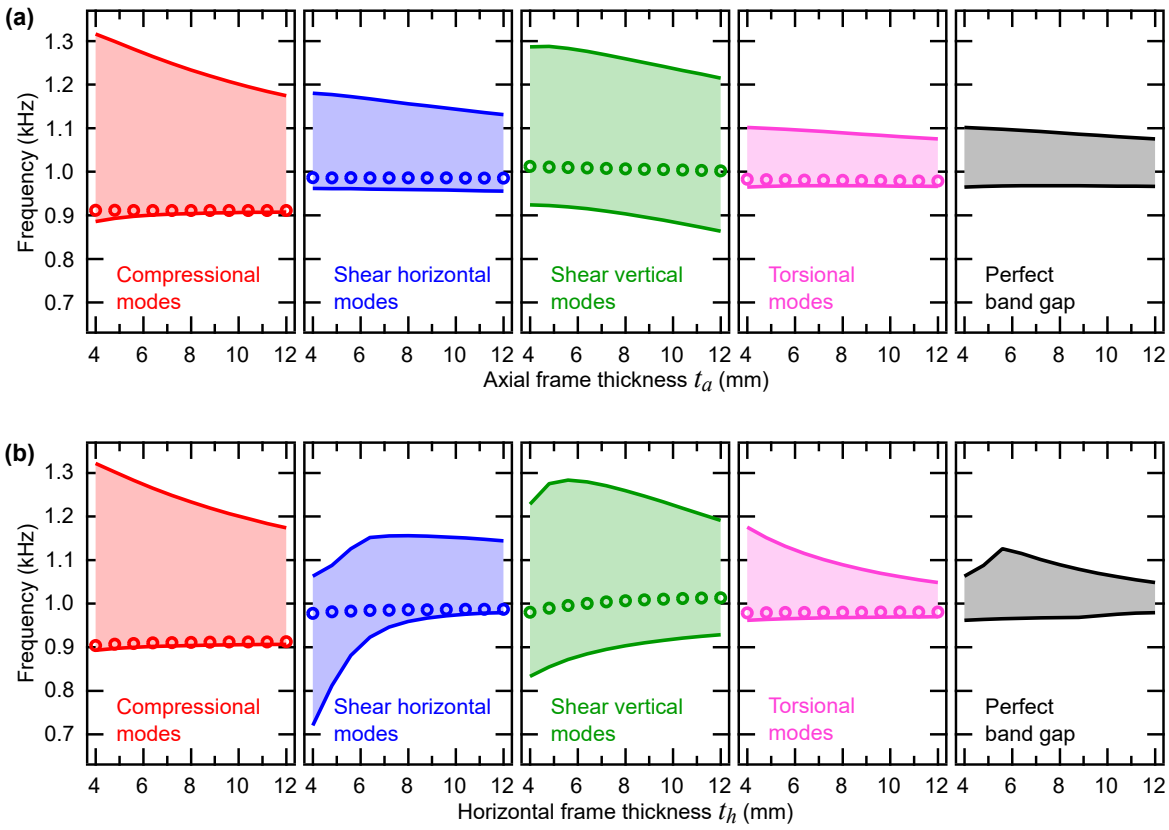

Figure S7: Simulated band gap variation with outer frame thicknesses. (a) and (b) indicate the effect of varying the axial and horizontal thicknesses t_a and t_h, respectively from their design value of 8 mm. The solid lines correspond to the top and bottom frequencies of each mode gap and the perfect band gap. The colored areas indicate inner gap frequencies. The open circles show eigenmodes calculated for a single unit cell with two fixed boundaries perpendicular to the axial direction.

narrower overall when t_a or t_h increase and the volume ratio of the inner resonator mass to the total unit cell area decreases. The band gap width for the torsional modes depends on t_h much more strongly than on t_a because this mode is sensitive to the horizontal dimensions. The shear-horizontal modes show a wider band gap than for the shear-vertical modes when t_h is small. The mismatch between the unit-cell frequencies and the onset of the band gaps is particularly evident when t_h is small, probably owing to the frame deformations.

3 Experimental setups

To efficiently detect a particular acoustic mode, the positions of the piezo plates and the directions of the analyzed accelerations are carefully chosen, as described below. Images of the experimental setups are shown in Fig. S8. The sample is suspended at two points by fishing line, and accelerometers are bonded at two points on each of the input and output sides. The piezo plate excites the vibrations, and is placed on the sample surfaces in three different ways. The piezo plate in Fig. S8(c) is bonded on the lower end face, and produces an axial force to excite compressional modes. The shear-horizontal modes are excited by bending forces along the width direction, as shown in Fig. S8(d). The shear-vertical modes and torsional modes are simultaneously excited and detected with the setup shown in Fig. S8(e).

The four acoustic modes are separately reconstructed from the measured acceleration amplitudes and a knowledge of the dominant displacement directions and their symmetry for each mode. In our experiments we only make use of the width-direction symmetry because we only made measurements on a single face. Measurements on the opposite face are not necessary because of the known acoustic mode symmetry. By considering the symmetry of the width-direction deformations, we classify the measured acceleration amplitudes, i.e. the axial-direction acceleration amplitudes and symmetric components for the compressional modes, the width-direction amplitudes and antisymmetric components for the shear-horizontal modes, the depth-direction amplitudes and symmetric components for the shear-vertical modes, and the depth-direction amplitudes and antisymmetric components for the torsional modes.

4 Details of the simulations

The finite-element numerical simulations are conducted with COMSOL Multiphysics version 5.4. The acoustic eigenmodes of a single cell and the dispersion relations are derived by eigenfrequency studies with the Solid Mechanics interface that solves the equations of motion for elastic bodies. A region making up one quarter of a unit cell is simulated, and use is made of the mode symmetry, either symmetric or antisymmetric (see Table I in the main text). For these simulations a total of ∼8,500 triangular-prism mesh elements are used, and the maximum and minimum element sides are 2 and 0.7 mm, respectively. Rigid boundary conditions or Floquet periodic boundary conditions are used to derive the eigenmodes of a single cell or the dispersion relation, respectively, and are applied on the boundaries of the unit cell perpendicular to the axial direction.

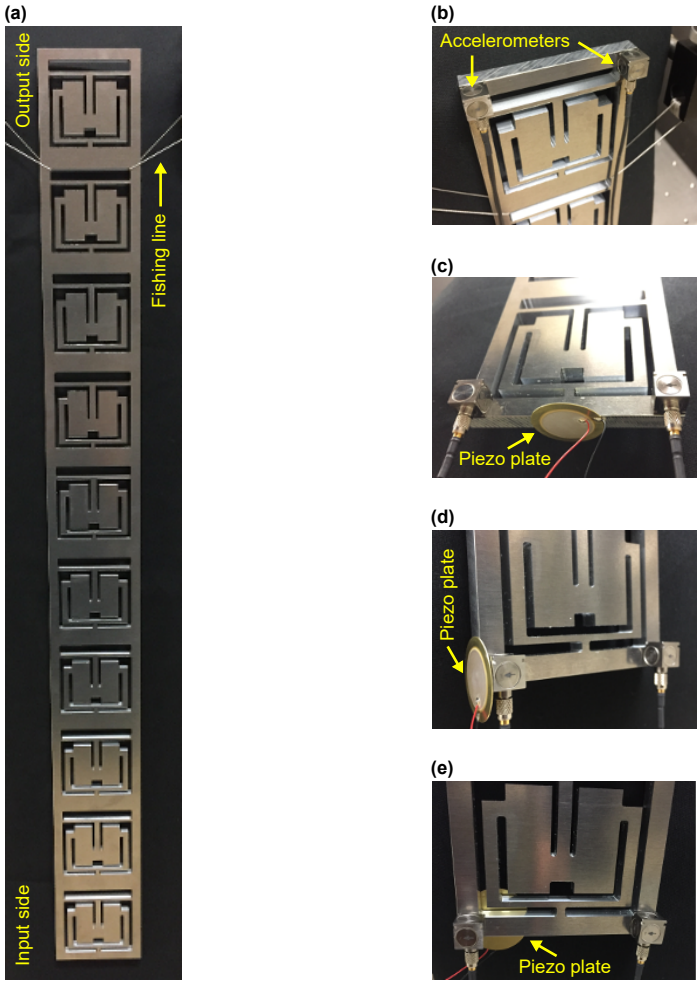

Figure S8: Images of the experimental setups used for detection of the different acoustic polarizations. (a) A meta-beam suspended by fishing line before attaching accelerometers and piezo plates. (b) Output-side setup. (c), (d) Input-side setups for compressional mode or shear-horizontal mode investigations, respectively. (e) Input-side setup for shear-vertical or torsional mode investigations. The piezo plate is positioned on the opposite face to the accelerometers.

In the simulations for the decay constants for a beam of 10 unit cells in length, we again simulate a quarter of each unit cell, and work in the frequency domain with a 5 Hz step. A total of ∼85,600 triangular-prism mesh elements are used, with a size similar to that mentioned above. To efficiently excite each acoustic mode, four types of loads are applied on the end face of the meta-beam, as described in the main text. Particular components of the acceleration for each mode are selected for analysis on the upper right-hand edge of the meta-beam, as described in Fig. 6(a) of the main text. For compressional modes, a uniform axial force is applied, and the axial acceleration is analyzed. For shear-horizontal and -vertical modes, a uniform force is applied parallel to the meta-beam end face and along the width and depth directions, respectively; the same directions of the acceleration component are selected for analysis. For the torsional modes, an axial torque is applied to the meta-beam end face, which rotates about the axial direction, and the out-of-plane component of the acceleration is analyzed. The accuracy of the simulations were checked by using different discretizations. The decay constant is defined as the distance over which the acoustic amplitude is expected to decay by $1/e$.

References

[1] S. P. Timoshenko, *History of Strength of Materials, with a Brief Account of the History of Theory of Elasticity and Theory of Structures* (McGraw-Hill, 1953).

[2] S. P. Timoshenko and J. N. Goodier, *Theory of Elasticity,* 3rd ed. (McGraw-Hill, 1970).